

See discussions, stats, and author profiles for this publication at: <https://www.researchgate.net/publication/350446191>

Design and optimization of bump (compression surface) for diverterless supersonic inlet

Article in *Proceedings of the Institution of Mechanical Engineers Part G Journal of Aerospace Engineering* · March 2021

DOI: 10.1177/09544100211002970

CITATIONS

4

READS

343

3 authors:



Irsalan Arif

The Hong Kong Polytechnic University

37 PUBLICATIONS 92 CITATIONS

SEE PROFILE



Hassan Iftikhar Hashmi

The Hong Kong Polytechnic University

18 PUBLICATIONS 146 CITATIONS

SEE PROFILE



Ali Javed

National University of Sciences and Technology

50 PUBLICATIONS 280 CITATIONS

SEE PROFILE

Design and optimization of bump (compression surface) for diverterless supersonic inlet

Proc IMechE Part G:
J Aerospace Engineering
2021, Vol. 0(0) 1–16
© IMechE 2021
Article reuse guidelines:
sagepub.com/journals-permissions
DOI: 10.1177/09544100211002970
journals.sagepub.com/home/pig

Irsalan Arif¹, Hassan Iftikhar² and Ali Javed³

Abstract

In this article design and optimization scheme of a three-dimensional bump surface for a supersonic aircraft is presented. A baseline bump and inlet duct with forward cowl lip is initially modeled in accordance with an existing bump configuration on a supersonic jet aircraft. Various design parameters for bump surface of diverterless supersonic inlet systems are identified, and design space is established using sensitivity analysis to identify the uncertainty associated with each design parameter by the one-factor-at-a-time approach. Subsequently, the designed configurations are selected by performing a three-level design of experiments using the Box–Behnken method and the numerical simulations. Surrogate modeling is carried out by the least square regression method to identify the fitness function, and optimization is performed using genetic algorithm based on pressure recovery as the objective function. The resultant optimized bump configuration demonstrates significant improvement in pressure recovery and flow characteristics as compared to baseline configuration at both supersonic and subsonic flow conditions and at design and off-design conditions. The proposed design and optimization methodology can be applied for optimizing the bump surface design of any diverterless supersonic inlet system for maximizing the intake performance.

Keywords

Bump, diverterless supersonic intake, pressure recovery, supersonic flow

Date received: 23 May 2020; accepted: 20 February 2021

Introduction

The propulsion system of supersonic jets requires an optimized airflow with minimum distortion through engine inlet to enable the aircraft operations in an extensive range of flight envelope at supersonic speeds. The modern day aircraft are equipped with inlet systems which are designed to provide higher pressure recovery while maintaining minimum flow distortion levels.^{1,2} Different approaches and methods have been reported in literature for the design of inlet systems based on flow characteristics, geometric modifications, and compression regimes.^{3,4} Conventional designs of inlet systems comprise boundary layer (BL) diverters in conjunction with other moving parts like shock cones and variable ramps, making the design heavy and resource-demanding. The fixed and moving parts consisting of diverters, splitter plates, and bleed control systems make the entire inlet system rather complex.⁵ Recently, a relatively new concept of intake, namely the diverterless supersonic intake (DSI) system, has been introduced based on application of a three-dimensional fixed surface (bump) as a replacement of the diverter-based inlet system. The bump surface along with inlet cowl is found to be instrumental in diverting the

upstream BL and creating air compression for the inlet system.^{6,7} Diverterless supersonic intake has gained significant importance in aircraft intake design due to its favorable characteristics including weight reduction, pressure recovery, and low flow distortion as compared to other conventional intakes. Diverterless supersonic intake requires only non-moveable three-dimensional surface while maintaining all the benefits of a diverter-based systems. The integration of DSI requires a well-designed bump (compression surface) which provides BL diversion and ensures smooth flow inside the intake duct.

¹ Department of Mechanical Engineering, The Hong Kong Polytechnic University, Kowloon, Hong Kong

² School of Design, The Hong Kong Polytechnic University, Kowloon, Hong Kong

³ Department of Aerospace Engineering, College of Aeronautical Engineering, National University of Sciences & Technology, Islamabad, Pakistan

Corresponding author:

Irsalan Arif, Department of Mechanical Engineering, The Hong Kong Polytechnic University, Hung Hom, Kowloon 999077, Hong Kong.
Email: irsalan.arif@connect.polyu.hk

The concept of three-dimensional compression surface was introduced by Seddon and Goldsmith.⁴ Hamstra and Sylvester⁶ proposed the design of a diverterless inlet system and investigated the functional capacity of bump and claimed it as a feasible alternative of BL diverters, BL bleed systems, and splitter plates. Since then, a number of studies have been carried out to investigate the effectiveness of DSI in BL diversion and performance improvement of the intake system. The flow dynamics over the bump surface and the behavior of upstream BL diversion were investigated in a wind tunnel experiment at Mach 3.0 by Tillotson et al.⁸ A comparison of the forebody bump inlet system with the forebody ramp inlet system has also been investigated at a range of Mach numbers from 1.5 to 2.0 while enunciating the advantage of DSI over diverter-based inlets by Simon et al.⁹ Various computational studies have been carried out to investigate the different three-dimensional inlet bumps for shock–boundary–layer interactions (SBLI) and analyze the performance at different Mach numbers.^{10–12} Owing to its superior design, DSI has been regarded as a favorable choice for several modern supersonic jet aircraft.¹³ The generation of bumped surface requires a modern and robust design methodology as it needs to actively divert the upstream BL while maintaining the pressure recovery with minimum drag spillage. Stream tracing technique can be considered as one of the generation methods for bump alternatively known as raised compression surface.^{4,6,14,15} This technique has certain limitations at low supersonic speeds as the implementation of the design framework is confounded by the change in shock patterns. Such variations in shock patterns require an additional surface and trimming to effectively divert the SBLI. Other studies¹⁶ have analyzed the bump surface designed by the stream tracing technique in a tunnel test of subscaled aircraft models along with the computational fluid dynamic simulations. The investigations have demonstrated the effects of shock patterns at the entrance of the supersonic inlet system.

Although a significant amount of research has been carried out to analyze the performance of DSI in diverting the BL at different flow conditions, evaluation of design characteristics of bump surface for DSI is still an active area of research. The literature reports favorable characteristics of DSI in terms of pressure recovery and flow distortion at different flow speeds and angles of attack.^{5,17,18} However, no information regarding the design parameters of the bump surface is available. It is still unknown whether the existing bump surfaces for DSI are optimized to provide maximum possible pressure recovery at design conditions or not. Moreover, the design process of bump surface for an integrated DSI system is evolving and requires further study.

This study aims to develop a design and optimization scheme for a three-dimensional bump surface by analyzing different design parameters of bump (compression surface) for the DSI system. The developed scheme can be utilized to design a new bump surface or to improve an existing bump surface for a DSI system. Computational

design and numerical analysis are carried out to investigate the performance of bump surfaces along with forward cowl inlet duct based on pressure recovery and flow characteristics at supersonic flow conditions. Initially, a baseline bump is modeled in accordance with an existing bump configuration on a supersonic jet aircraft and the numerical scheme is validated with results reported in literature. Bump design is based on five parameters including bump initial angle, bump final angle, maximum amplitude of bump, location of max amplitude on the longitudinal axis, and bump axisymmetric location. Design space is established using sensitivity analysis to identify the uncertainty associated with each design parameter by the one-factor-at-a-time (OFAT) approach and eliminating the nonsensitive parameters from the design space. Subsequently, a three-level design of experiments (DOE) is performed using the Box–Behnken method, and the computational analysis is carried out at 25 selected designed configurations. Surrogate modeling is carried out by the least square regression method (LSRM) to define the fitness function, and optimization is performed using genetic algorithm (GA) based on pressure recovery as the objective function.

The article is organized as follows. Design and modeling of bump configuration and intake duct are presented in Section 2. The details of the computational setup and numerical modeling are presented in Section 3. A brief on validation of numerical scheme with literature is also presented in this section. Section 4 presents a detailed optimization process including determination of design space using OFAT sensitivity analysis, three-level DOE using Box–Behnken method, and design of an optimized bump configuration based on GA. Subsequently, a detailed analysis of optimized bump configuration is presented along with comparison of baseline bump configuration.

Modeling of bump and intake

For the present study, the three-dimensional bump geometries are modeled by hyperbolic approximation for the cone flow streamlines.⁴ Usually, the three-dimensional bump geometry is based on the characteristics of cone flow. The relieving effect for the cone is different from a two-dimensional wedge which forms a stronger shock than the three-dimensional cone.¹⁹ The mathematical formulation for modeling of three-dimensional bump geometry presented by Sedon⁴ is utilized in this study. Figure 1 shows the geometric parameters considered for the design of three-dimensional bump geometry. The equations of the plane with shock angle β are expressed as

$$x = h \cot \beta \sec \theta; \quad y = h \tan \theta; \quad z = \frac{x \tan \beta}{\sec \theta} \quad (1)$$

$$\begin{aligned} x^2 \tan^2 \beta - y^2 &= h^2 \\ y &= h \tan \theta \end{aligned} \quad (2)$$

The equations for the intersection of the plane and shock surface are expressed as

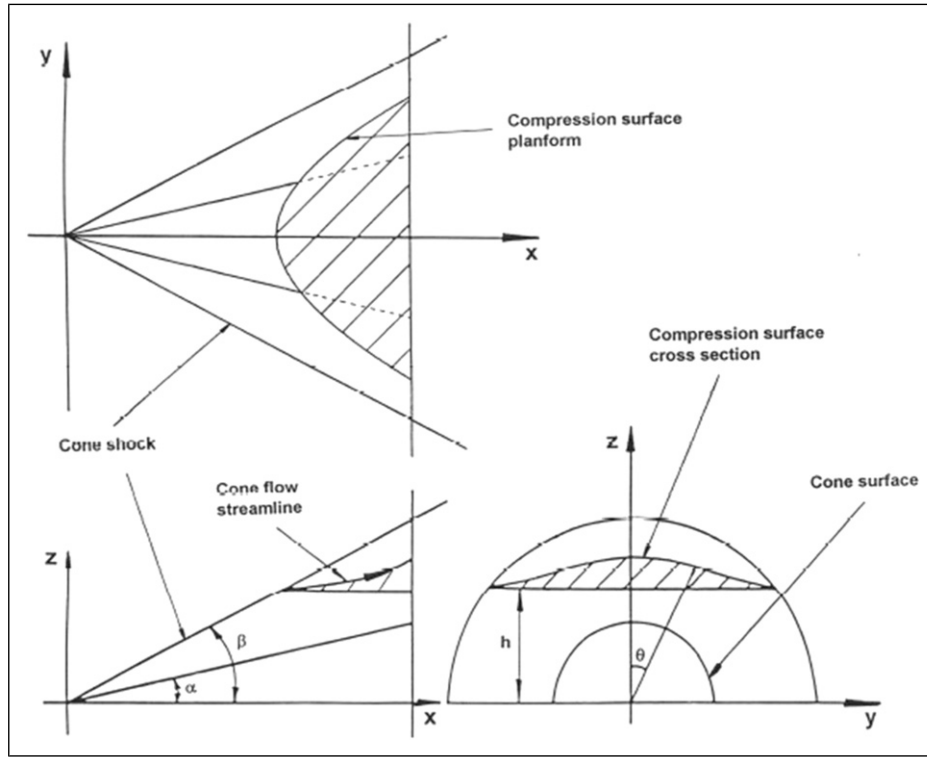


Figure 1. Bump geometric parameters.

$$x = h \cot \beta \sec \theta; \quad y = h \tan \theta; \quad z = \frac{x \tan \beta}{\sec \theta} \quad (3)$$

The streamline for generation of bump is defined by

$$r^2 = z^2 \sec^2 \theta = x^2 \tan^2 \alpha + c \quad (4)$$

Finally, the streamline equation is then solved for the z-coordinate to create the bump geometry by

$$z = \sqrt{\frac{x^2 \tan^2 \alpha + c}{\sec^2 \theta}} = \frac{\sqrt{x^2 \tan^2 \alpha + c}}{(1/\cos(\tan^{-1} 1/h))^2} \cdot A \times B \quad (5)$$

Here, α is the cone angle and c is a constant. To design the modified bump geometries for this study, the trigonometric variable $A = (x)$ and magnitude variable B are incorporated in equation (5). The designed geometries are further made compatible for numerical analysis by smoothing functions.

Six different design parameters including initial bump angle, transitional bump angle measured at 30% of bump length from the longitudinal axis, final bump angle, maximum amplitude of bump, location of maximum amplitude in the longitudinal axis, and bump axisymmetric location about the y -axis have initially been chosen to design bump geometry as defined in Figure 2. The maximum amplitude and location of maximum amplitude of bump are normalized by the total length of bump. The overall perimeter (length and width) of the bump surface is fixed according to the inlet cowl and existing bump configuration on a fighter aircraft. The

selected design parameters can define any three-dimensional bump geometry. Hence, these parameters can be used for design and optimization process for bump design for any DSI system.

The three-dimensional bump geometry is incorporated with a forward-swept intake cowl and a duct. The length of duct, the height of intake cowl, and location of the inlet lip are fixed corresponding to bump location. For the present study, we have not considered a Y-shaped duct as utilized in^{5,16} which generally results in BL separation at the sharp bends and can result in flow distortion and performance degradation at certain flow conditions. Since this study aims to design and optimize a three-dimensional bump surface, a simpler duct geometry would help in much accurate analysis. The size of the duct is considered similar to the work of¹³ with an lift to drag ratio of 5.4. Furthermore, a planar geometry is considered at upstream of bump instead of aircraft nose geometry; as for the flow condition considered in this study, the upstream BL would be similar for all bump configurations; hence, a complex upstream geometry of aircraft nose would rather complicate the process of grid consistency for all bump geometry cases as discussed in Section 3.2. Optimization of duct shape and upstream geometry is out of scope of this research. Furthermore, the developed optimization scheme can later be applied to any bump and duct combination. Figure 3 shows side, front, and isometric views of consolidated bump and intake geometry. The wireframe of the inlet duct is also shown in Figure 3(d).

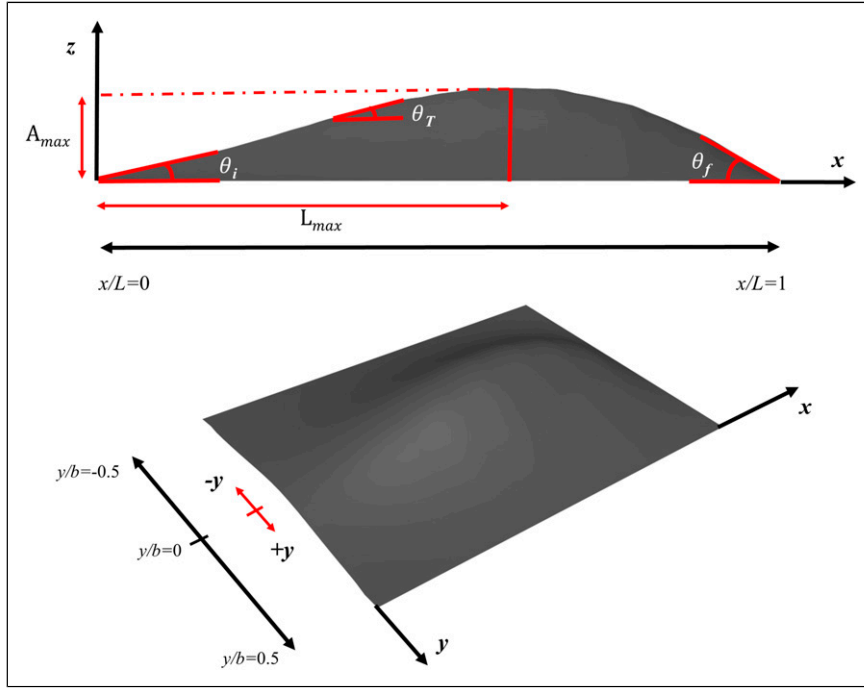


Figure 2. Bump geometry and definition of bump design parameters.

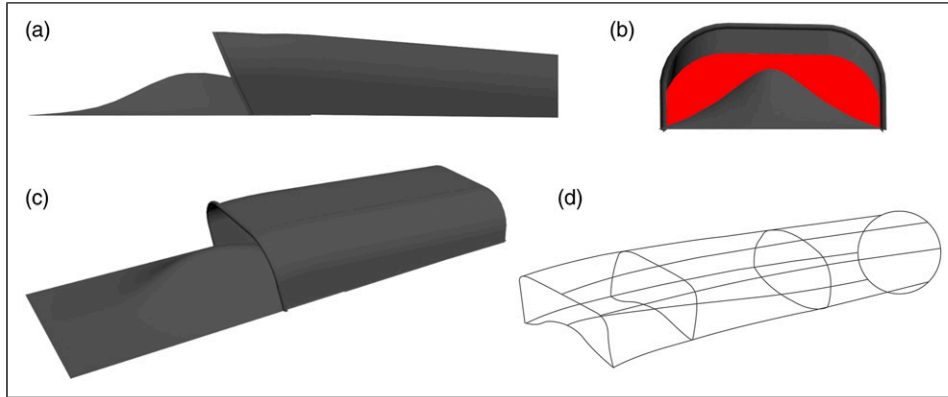


Figure 3. Bump and intake duct. (a) side view; (b) front view; (c) perspective view; and (d) wireframe of inlet duct.

Computational setup and numerical modeling

Numerical approach (equations)

For numerical analysis, Reynolds-averaged Navier–Stokes (RANS) set of equations are used to account for the time-dependent behavior of flow.²⁰ Reynolds-averaged Navier–Stokes equations help in optimum utilization of computational resources by averaging the flow quantities over the entire range of turbulence scale.²¹ Reynolds-averaged Navier–Stokes equations also cater for Reynolds stressors that form an important part of flow analysis. The governing conservation equations are the following:

Conservation of mass

$$-\frac{\partial \rho}{\partial t} = \frac{\partial(\rho u)}{\partial x} + \frac{\partial(\rho v)}{\partial y} + \frac{\partial(\rho w)}{\partial z} \quad (6)$$

Conservation of momentum

$$\begin{aligned} \rho \left(\frac{\partial u}{\partial t} + u \frac{\partial u}{\partial x} + v \frac{\partial u}{\partial y} + w \frac{\partial u}{\partial z} \right) \\ = -\frac{\partial p}{\partial x} + \mu \left(\frac{\partial^2 u}{\partial x^2} + \frac{\partial^2 u}{\partial y^2} + \frac{\partial^2 u}{\partial z^2} \right) + F_x \end{aligned} \quad (7)$$

$$\begin{aligned} \rho \left(\frac{\partial v}{\partial t} + u \frac{\partial v}{\partial x} + v \frac{\partial v}{\partial y} + w \frac{\partial v}{\partial z} \right) \\ = -\frac{\partial p}{\partial y} + \mu \left(\frac{\partial^2 v}{\partial x^2} + \frac{\partial^2 v}{\partial y^2} + \frac{\partial^2 v}{\partial z^2} \right) + F_y \end{aligned} \quad (8)$$

$$\rho \left(\frac{\partial w}{\partial t} + u \frac{\partial w}{\partial x} + v \frac{\partial w}{\partial y} + w \frac{\partial w}{\partial z} \right) = -\frac{\partial p}{\partial z} + \mu \left(\frac{\partial^2 w}{\partial x^2} + \frac{\partial^2 w}{\partial y^2} + \frac{\partial^2 w}{\partial z^2} \right) + F_z \quad (9)$$

Conservation of energy

$$\rho C_p \left(\frac{\partial T}{\partial t} + u \frac{\partial T}{\partial x} + v \frac{\partial T}{\partial y} + w \frac{\partial T}{\partial z} \right) = \Phi + \frac{\partial}{\partial x} \left[k \frac{\partial T}{\partial x} \right] + \frac{\partial}{\partial y} \left[k \frac{\partial T}{\partial y} \right] + \frac{\partial}{\partial z} \left[k \frac{\partial T}{\partial z} \right] \quad (10)$$

where

$$\begin{aligned} \Phi = & 2\mu \left[\left(\frac{\partial u}{\partial x} \right)^2 + \left(\frac{\partial v}{\partial y} \right)^2 + \left(\frac{\partial w}{\partial z} \right)^2 + 0.5 \left(\frac{\partial u}{\partial y} + \frac{\partial v}{\partial x} \right)^2 \right. \\ & + 0.5 \left(\frac{\partial v}{\partial z} + \frac{\partial w}{\partial y} \right)^2 + 0.5 \left(\frac{\partial w}{\partial x} + \frac{\partial u}{\partial z} \right)^2 \left. \right] \\ & - \frac{2}{3}\mu \left(\frac{\partial u}{\partial x} + \frac{\partial v}{\partial y} + \frac{\partial w}{\partial z} \right)^2 \end{aligned}$$

Where ρ is the fluid density, μ is the kinematic viscosity, u, v , and w are the three Cartesian component of flow velocity, p is the pressure term, F_x, F_y , and F_z are the body force terms, T is the temperature, and k is the heat transfer coefficient. Solution of governing equations is sought using control volume-based numerical solver. Double precision solver is used for high accuracy and fluid is taken as air with ideal gas properties. Density-based solver is selected with explicit algorithm, and second-order upwind scheme is selected in flow discretization and first-order upwind scheme is used to cater for turbulent viscosity. Suitable relaxation parameters are applied to control the solution stability. A rectangular computational domain is modeled with the upstream located at 5 duct lengths to model freestream conditions and to avoid any influence of pressure field around the bump or inlet. The domain is selected as pressure far field with suitable inputs for freestream conditions. All surfaces of bump, fuselage, and intake duct are selected as no-slip walls. The aerodynamic interface plane (AIP) has been modeled as outlet with controlled mass flow rate to simulate the exact flow characteristics in accordance to the engine requirements. The duct outlet surface has also been utilized for calculation of pressure recovery and distortion coefficient (DC) as indicated in Figures 3(a)–(d). The analysis is carried out at design mass flow rate (DMFR), low mass flow rate (LMFR), and high mass flow rate (HMFR) which are determined from the in-house analytical engine model developed by the author.²²

Solution strategy

For numerical analysis, the accuracy of results greatly depends on the mesh structure and quality. Since the present study requires analysis of different bump geometries

based on multiple design parameters, it is imperative to maintain the mesh consistency for all simulation cases. Hence, we employed a unique solution strategy of geometric assembling/append approach where the designed bump geometry with inlet cowl is embedded in a separate sub-domain and appended with the primary domain as shown in Figure 4(a). This feature helps in the numerical analysis of different bump geometries by just incorporating the sub-domain (consisting of different designed bumps) in the primary domain without affecting the overall geometry and thus maintaining the mesh consistency for all bump geometries. Although the employed scheme is complex in its implementation due to the presence of multiple sub-domains and requires prior planning in domain modeling/interfaces, it serves two major purposes. First, the numerical solution of the intake system with baseline bump geometry can be simulated until the flow variables are stabilized. Subsequently, designed bump geometry is appended and the solution is progressed which saves computational time/cost by 60%. Second, the mesh consistency remains unaffected for all bump geometries to ensure high accuracy in numerical solutions.

Grid generation and independence study

Grid generation is one of the key steps in numerical simulation. It is imperative to design and implement a smart grid scheme which is dense and fine enough to capture all flow phenomena accurately. However, this aspect needs to be balanced with available computational resources and time. For this study, we have employed a hybrid mesh scheme where the bump and duct geometries are meshed separately by unstructured mesh elements using elliptical refinement to maintain grid orthogonality at the surfaces and improve solution accuracy in near-wall region. Special emphasis has been laid to ensure that the sharp curves and important features such as duct forward lip and bends are meshed with fine refined mesh (Figure 4(b)). For these surfaces, a bottom-top approach is employed where the edge sizing is applied and subsequently face sizing is applied to control the mesh elements accordingly. A minimum mesh element size in streamwise coordinate $\Delta x = 1.71 \times 10^{-4}$ is set near the aircraft surfaces, whereas in the vertical direction, the minimum mesh element size is set to $\Delta y = 2.3 \times 10^{-5}$. The grid size is gradually increased away from the surfaces utilizing the inflation features for optimal computational requirements. A multilayer prism is also applied on the bump and duct to accurately capture BL and near-wall effects. A total of 20 prism layers are applied on the bump and duct surfaces to analyze the BL characteristics and its associated unsteadiness precisely. The layers are inflated with a ratio of 1.001 until twice the size of local BL thickness δ^+ is achieved. The turbulent y^+ values are kept at an optimum level of less than 1 at boundary surfaces as shown in Figure 4(c). Prime importance is given to maintain mesh consistency at all simulating conditions. Three different meshes are generated, namely G1 (5.4 million), G2 (7.7 million), and G3 (8.9 million), based on

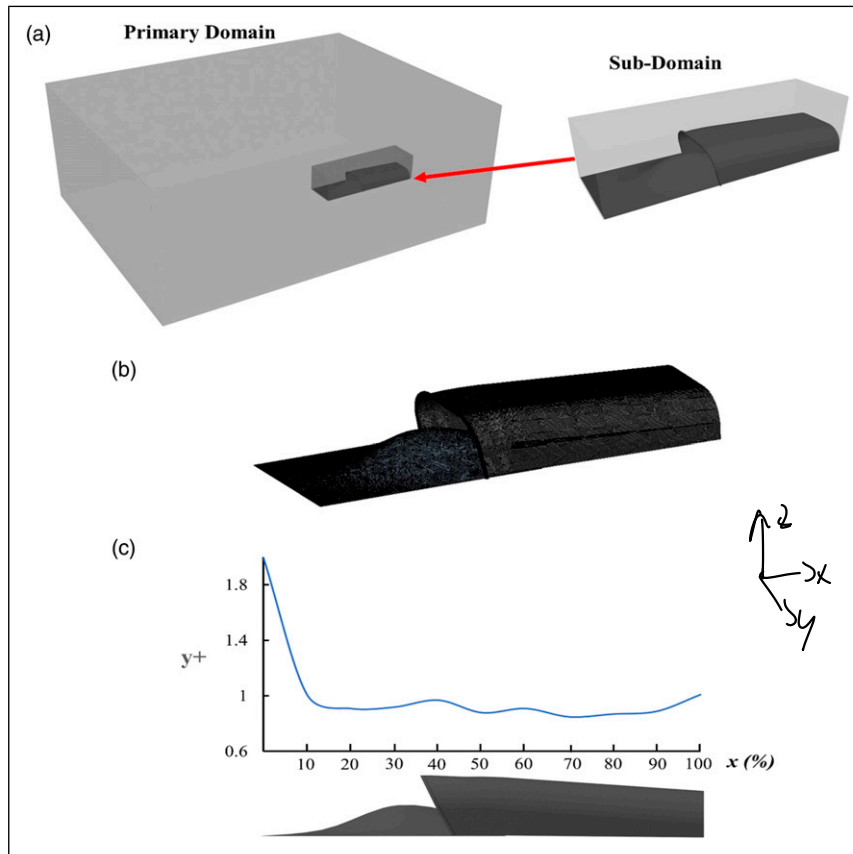


Figure 4. (a) Primary domain and sub-domain; (b) meshed bump and duct; and (c) $y +$ distribution on the intake system.

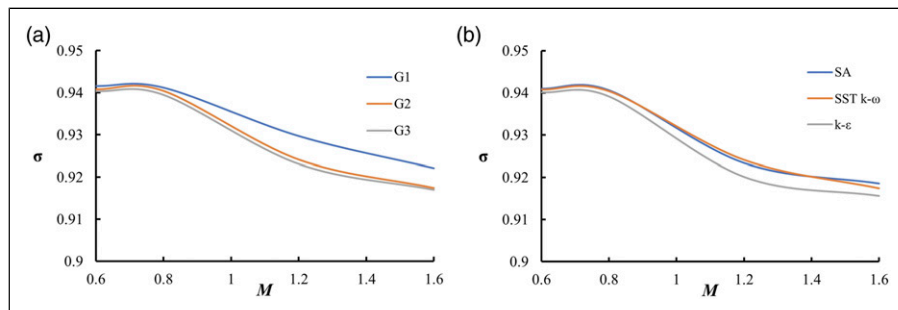


Figure 5. (a) Grid independence and (b) turbulence model independence.

the number of cells. Grid G2 is generated by refining the near-wall grid parameters of G1 by a factor of 0.8, whereas G3 is generated by further refining the near-wall grid size of G2 by a factor of 0.85. In order to select an optimum mesh size, a grid independence study is carried out at different flow speeds and DMFR for optimum grid selection. For this purpose, the pressure recovery is evaluated for all three grids at different flow speeds. Pressure recovery ' σ ' is defined as

$$\sigma = \frac{P_{T,AIP}}{P_{T,\infty}} \quad (11)$$

where AIP is the aerodynamic interface plane. From Figure 5(a), it is observed that a negligible difference is observed for calculated pressure recovery at the subsonic condition for all grids; however, at supersonic speed,

a significant deviation in pressure recovery for G1 is observed, whereas the pressure recovery for G2 and G3 are almost similar. Therefore, grid G2 is selected for further analysis based on the balance between accuracy and the required computational resources.

The selection of turbulence model is as important as selection of grid size for numerical analysis; hence, this aspect cannot be ignored. For this research, three different models (Spalart-Allmaras turbulence model (SA), shear stress transport turbulence model (SST) k- ω , and k- ϵ) are analyzed based on grid G2. Spalart-Allmaras turbulence model is a single equation turbulence model, while k- ϵ and SST k- ω are two-equation turbulence models.^{23,24} Comparative results of pressure recovery for these models are presented in Figure 5(b). Based on the results, it is observed that the variation of pressure recovery obtained

from SA model and SST $k-\omega$ model is almost negligible; however, the results obtained from $k-\epsilon$ are underpredicted for all flow speeds. Also, the convergence stability and residuals from SA and $k-\epsilon$ are not satisfactory, as disordered sinusoidal behavior is observed throughout the simulations. Hence, SST $k-\omega$ turbulence model is selected for this research since it is a two-equation turbulence model which in addition to the conservation equations solves two transport equations that account for the history effects such as convection and diffusion of turbulent energy. The two transported variables are turbulent kinetic energy (k), which determines the energy in turbulence, and specific turbulent dissipation rate (ω), which determines the rate of dissipation per unit turbulent kinetic energy. Furthermore, the $k-\omega$ SST model provides a better prediction of flow separation than most RANS models and also accounts for its accuracy in adverse pressure gradients. It has the ability to account for the transport of the principal shear stress in adverse pressure gradient BL. The turbulence model is ideally suited for the current flow conditions which involves turbulence in the near vicinity of inlet duct and bump.

Results and discussion

The analysis is divided into 3 major parts. In the first part, analysis of baseline bump configuration is carried out at different mass flow rates for a supersonic speed of $M = 1.6$ and zero angle of attack. The numerical scheme is subsequently validated with available literature. In the second part, analysis of different bump geometries is carried out at supersonic speed of $M = 1.6$, and the developed optimization scheme is employed to ascertain the optimum configuration based on pressure recovery as the objective function. In the final part, the optimized configuration is modeled and analysis is carried out at different mass flow rates to analyze its performance and a comparative analysis with baseline bump is also presented. The total pressure at AIP is determined by mass-weighted average over the outlet face. Simulations are progressed for an adequate time until the numerical variables are sufficiently converged based on a stringent convergence criterion. The values of all the flow variables utilized for the analysis are based on the mass-weighted average extracted from the numerical solution.

Analysis of baseline configuration and validation of solution scheme

Analysis of baseline configurations is carried out initially to validate the proposed solution scheme and methodology. Furthermore, the baseline configuration would help in setting up the design space for subsequent optimization study. The design parameters of baseline bump configuration are set in accordance with an existing bump configuration on a supersonic jet aircraft. Table 1 shows the design parameters considered for baseline bump configuration. We evaluated the pressure recovery at DMFR, low mass flow rate (LMFR = 80% DMFR), and high mass flow

Table 1. Parameters for baseline configuration.

Case	θ_i	θ_f	A_{\max} (z/L)	L_{\max} (x/L)	γ
Baseline	21°	26°	0.135	0.55	0

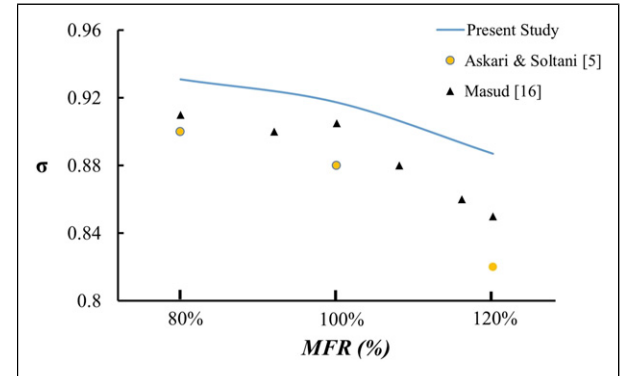


Figure 6. Comparison of calculated pressure recovery with literature.

rate (HMFR = 120% of DMFR) at $M = 1.6$ for validation purpose. The pressure recovery evaluated by Masud¹⁶ and Askari & Soltani⁵ are also plotted in Figure 6. Due to the variations in the duct shape of present study and Masud¹⁶ and Askari & Soltani,⁵ the results are qualitatively compared only to analyze the trend of pressure recovery with the change in MFR of our study with the literature. Since the exact mass flow rates are uncertain for both these research, approximate values are evaluated for LMFR and HMFR conditions. An excellent agreement between the overall trend is observed for our numerical scheme with literature where the pressure recovery is found to moderately decrease with an increase in mass flow rate until a sharp drop in pressure recovery is observed at HMFR for all analyses. Hence, from the analysis shown above, the selected numerical methods, grid size, and turbulence model are considered appropriate for the numerical simulations in the present research.

Optimization

Design space and uncertainty analysis. The design of bump geometry is based on five different parameters which can result in a large number of possible configurations n^r , where r is the number of parameters (5 in the present study) and n is the number of variations in each parameter. Therefore, in view of the required computational time and resources, it is not feasible to carry out numerical simulation for each configuration. Hence, a sensitivity analysis is initially performed to determine the effect of each parameter on intake performance. Furthermore, sensitivity analysis can also help in identifying the extent of uncertainty associated with each variable. Pressure recovery is chosen as the objective function for this study and OFAT approach is used for sensitivity analysis. This approach suggests the effect of varying the value of a single parameter while other parameters are fixed at baseline

values. The design experiment based on OFAT has been commonly employed in the aerospace industry ranging from wind tunnel tests to material compositions of the aircraft parts.^{25,26} The method is prevalent due to its ability to effectively anticipate the potential difficulties as well as maximizes the data acquisition rate. The basic requirement for OFAT is to identify the design space/range for each variable. The range of each parameter is carefully determined based on the physical features, flow characteristics, and physical limitations of bump design. A preliminary design space is established with all the parameters, and uncertainty analysis is carried out to identify the nonsensitive parameters and to setup a refined design space. The range of initial angle is taken from 19 to 31° based on the formation of shock structure. The minimum initial angle is chosen to avoid the ingestion of shock wave inside the inlet cowl, while the maximum angle is based on the physical limitation of geometry shape. The range of transition angle is set in accordance to the initial angle so that the maximum amplitude location can be reached smoothly at a fixed location. The transition angle is, therefore, not an independent parameter and is coupled with the initial angle for this study. The range of final bump angle is set between 21 and 36° to ensure smooth flow of air inside the duct without any significant flow separation toward the rear end of bump. The range of maximum amplitude of bump is taken from 0.121 to 0.15(z/L). Maximum amplitude of bump is limited by inlet

cowl height, choking condition, and mass flow rate requirement of intake. The range of location of maximum amplitude is taken from 0.5 to 0.65(x/L) which is relative to position of intake cowl lip in order to ascertain the effect of peak of bump on intake pressure recovery. The range of axisymmetric location of bump in y-axis is set from y = 0 to $\Delta y = \pm 5\%$ to ascertain the effect of bump location in y-axis. The initial design space selected for sensitivity analysis is shown in Table 2 (first row).

Figure 7(a) shows the variation in pressure recovery for initial angle and final angle at different variations within the design space. The variation in pressure recovery is found to be less than 1% at low angles (19–23°). However, a sudden drop in pressure recovery values is observed at high values of initial angles (23–31°). This is due to offsetting of shock wave structure from intake cowl lip. Therefore, the range of initial angle range is redefined from 19 to 23° to obtain the optimum results. The variation in pressure recovery with final angle indicates a rise in pressure recovery at lower to moderate range, whereas a significant drop is observed at higher values of final angle (32–36°) due to the flow separation downstream of peak. Similar degradation in pressure recovery is observed with different variations in initial angle. Therefore, range of final angle is redefined as 31–36° in the final design space. The variation in pressure recovery with maximum amplitude of bump is shown in Figure 7(b). A gradual and sustained decline in pressure recovery is observed with an

Table 2. Initial and final design space.

Case	θ_i	θ_f	A_{\max} (z/L)	L_{\max} (x/L)	Δy
Initial design space	19°–31°	21°–36°	0.121–0.15	0.42–0.65	$\pm 5\%$
Finalized design space	19°–23°	21°–31°	0.121–0.15	0.5–0.6	Eliminated

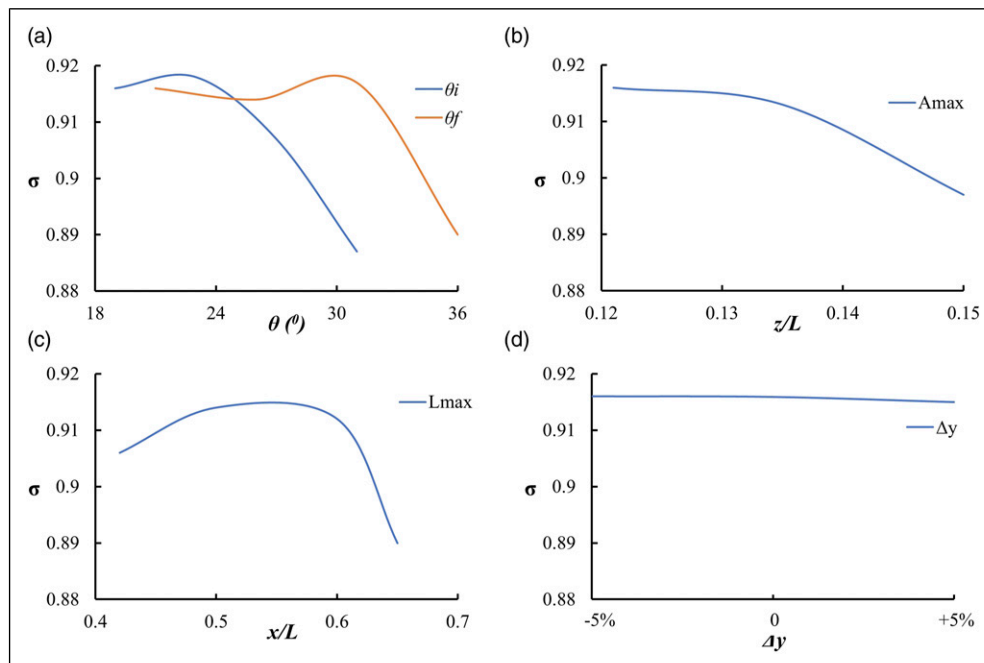


Figure 7. Sensitivity Analysis. (a) θ_i and θ_f ; (b) A_{\max} ; (c) L_{\max} ; and (d) Δy .

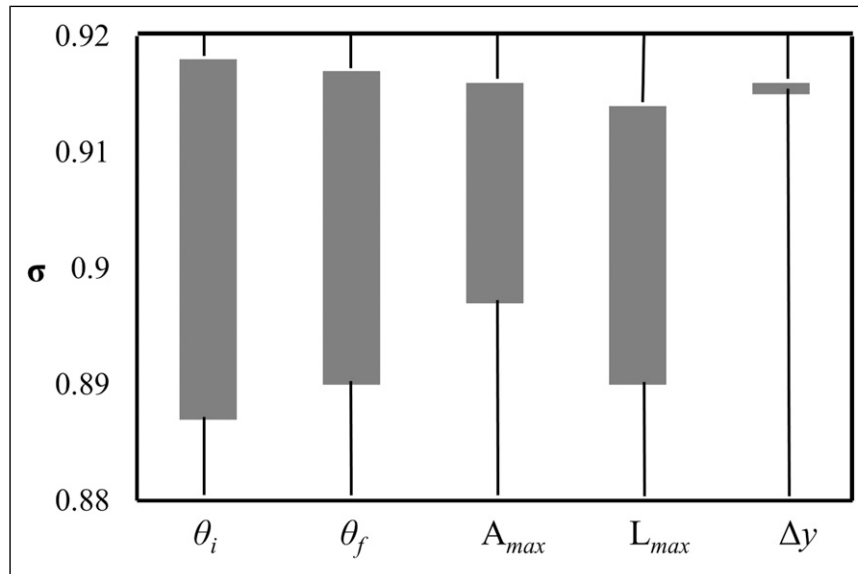


Figure 8. Box plot indicating total variation in pressure recovery for each parameter.

increase in peak amplitude. Therefore, the range of maximum amplitude of bump is kept unchanged. Figure 7(c) shows the variation of pressure recovery with the change in longitudinal location of bump peak. A non-uniform variation in pressure recovery is observed for values below 0.5 and above 0.6 (x/L) which further asserts the importance of the careful selection of this location in bump design. The revised range of values of longitudinal location of bump peak is set from 0.5 to 0.6 (x/L) in the final design space. Figure 7(d) shows that the variation in the axisymmetric location of bump is negligible which indicates that the flow behavior is unaffected with the slight shift in axisymmetric location. However, it may largely effect at higher offsets (15%–30%), but such high offsets are not physically desirable for any DSI system. For our range of ($\Delta y = \pm 5\%$), the difference is observed to be less than 0.5%. This implies that this design parameter may be excluded from optimization study.

To further illustrate the variation in pressure recovery for each design parameter, a box plot indicating the maximum and minimum value for each design variable is shown in Figure 8. It is evident that the bump axisymmetric location is insensitive to changes and results in minimum variation in pressure recovery, whereas the initial bump angle, final angle, maximum amplitude, and location of maximum amplitude have a significant influence on inlet performance. Based on OFAT and uncertainty analysis, the redefined design space for the optimization process is shown in Table 2.

DOE. Design of experiments is a systematic set of experiments scattered through the design space so as to establish a relationship between inputs and objective function. Design of experiments has proven instrumental in obtaining valid and unbiased conclusions.²⁷ A number of surrogate model-based optimization studies have applied this technique as it requires a small number of points

to delineate the design space effectively.²⁸ Since the current design space is based on four different parameters with variable ranges, it is impractical to carry out the numerical analysis of all possible combinations using full factorial design. Therefore, for the present study, Box–Behnken design²⁹ is used for response surface design to maximize the amount of information generated with a minimum number of simulations. A three-level DOE based on four factors is carried out with a single central point. A total of 25 experiments are designed by Box–Behnken DOE for four parameters. The designed set of experiments using Box–Behnken method is shown in Table 3. The baseline pattern is indicated by “0000,” whereas “+” indicates an increase in value of parameter and “−” sign indicates a reduction in variable value. The bump geometries based on the tabulated parameters are generated and meshed in a separate sub-domain. The bump sub-domain is later appended with the primary domain for high accuracy and consistency of results. All the computational setup and numerical parameters are kept same as already discussed in the subsection 4.2.1. The analysis is carried out at $M = 1.6$ and DMFR for all configurations. Table 3 also shows the evaluated ratio of intake throat to capture area ($A_{T/C}$), flow Mach number at AIP (M_{AIP}), and pressure (σ) for each configuration evaluated by numerical analysis. The $A_{T/C}$ is directly associated with the intake pressure recovery and flow speed within the duct. A higher $A_{T/C}$ indicates higher throat area which subsequently results in lower flow speed (M_{AIP}) inside the duct. However, the evaluated pressure recovery for each configuration is not linearly related to $A_{T/C}$ and M_{AIP} only and depends on other flow characteristics such as flow spillage and distortion. Hence, with specified DMFR, the calculated pressure recovery is a feasible indicator of intake performance based on different geometric bump parameters. It is interesting to note that higher pressure recovery is observed for some

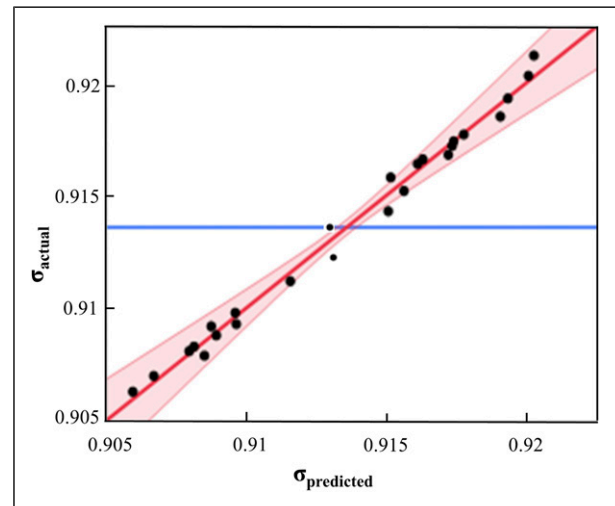
Table 3. Configurations by Box–Behnken design of experiments.

Pattern	θ_i (°)	θ_f (°)	A_{\max} (z/L)	L_{\max} (x/L)	$A_{T/C}$	M_{AIP}	Calculated σ
0000	21	26	0.135	0.55	0.735	0.401	0.9174
– 00 –	19	26	0.135	0.50	0.761	0.388	0.9156
+ – 00	23	21	0.135	0.55	0.741	0.398	0.9163
– + 00	19	31	0.135	0.55	0.734	0.402	0.9067
– – 00	19	21	0.135	0.55	0.745	0.396	0.9088
– 0 + 0	19	26	0.150	0.55	0.749	0.394	0.9080
– 00 +	19	26	0.135	0.60	0.729	0.404	0.9116
00 + –	21	26	0.150	0.50	0.773	0.383	0.9152
00 + +	21	26	0.150	0.60	0.727	0.406	0.9097
+ 0 – 0	23	26	0.121	0.55	0.749	0.394	0.9191
+ + 00	23	31	0.135	0.55	0.745	0.396	0.9081
00 – +	21	26	0.121	0.60	0.726	0.406	0.9178
+ 0 + 0	23	26	0.150	0.55	0.749	0.395	0.9172
0 – – 0	21	21	0.121	0.55	0.748	0.395	0.9173
0 + 0 +	21	31	0.135	0.60	0.715	0.411	0.9060
– 0 – 0	19	26	0.121	0.55	0.748	0.395	0.9193
0 + 0 –	21	31	0.135	0.50	0.769	0.385	0.9085
0 – + 0	21	21	0.150	0.55	0.782	0.379	0.9074
+ 00 +	23	26	0.135	0.60	0.716	0.411	0.9161
0 – 0 +	21	21	0.135	0.60	0.722	0.408	0.9096
0 – 0 –	21	21	0.135	0.50	0.778	0.381	0.9151
0 + – 0	21	31	0.121	0.55	0.740	0.399	0.9089
00 – –	21	26	0.121	0.50	0.779	0.380	0.9197
0 + + 0	21	31	0.150	0.55	0.717	0.411	0.9056
+ 00 –	23	26	0.135	0.50	0.784	0.378	0.9196

configurations (+0–0, 00– +, –0–0, 00, and +00–) than baseline bump configuration (pressure recovery = 0.9174) which indicates that a better design can be achieved with further optimization process.

Surrogate modeling. Once the numerical analysis of all 25 designed configurations has been performed, we subsequently perform the surrogate modeling to analyze the relationship between parameters and objective function. Least square regression method is utilized for said purpose due to its wide application and efficiency for the requisite estimation.³⁰ The LSRM by Longstaff and Schwartz³¹ has gained popularity among many aerospace researchers. LSRM tends to minimize the sum of the square of offsets and has high reliability. In the present study, a third-order polynomial fit is applied to the data to generate a response function. Figure 9 shows the actual versus predicted pressure recovery plot for applied LSRM where an excellent correlation is observed between the actual and predicted model. The R^2 is observed to be 0.99, and root mean square error (RMSE) of only 0.07% is observed which depicts an appropriate fitting model by LSRM. The fitness function obtained by LSRM is utilized for further optimization process.

Optimization Algorithm. For the optimization of bump design parameters, GA is implemented. The method is

**Figure 9.** Least square regression method depicting actual versus predicted pressure recovery.

widely used in the optimization process for engineering applications and has proven to be an efficient optimization process in the field of aerospace engineering as well.³² genetic algorithm applications have been successfully employed in a number of studies on spacecraft controls,³³ flight trajectories,³⁴ airfoil,^{35,36} and propellers.³⁷ For the present study, we preferred GA over gradient-based

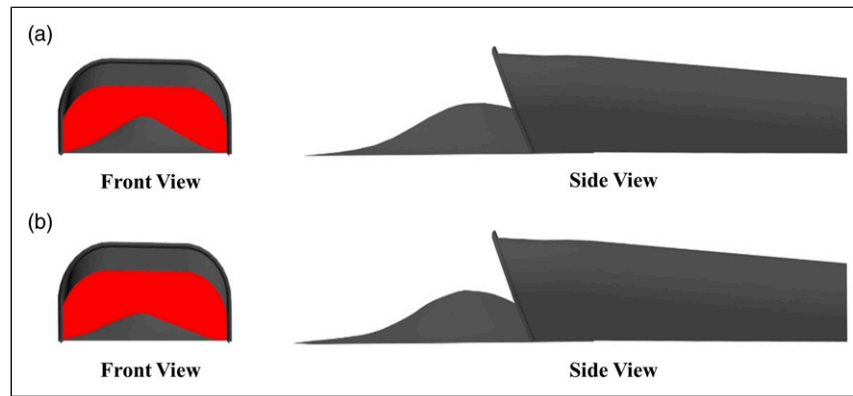
Table 4. Input parameters for genetic algorithm.

Attribute	Value	Attribute	Value
Population	200	Mutation	Adaptive feasible
Selection function	Stochastic	Scaling	Rank
Crossover	Double point	Function tolerance	1×10^{-10}

Table 5. Parameters for different configurations.

Case	θ_i	θ_f	A_{\max} (z/L)	L_{\max} (x/L)	$A_{T/C}$	M_{AIP}	DC	$C_{D_{split}}$	σ
Baseline	21°	26°	0.135	0.55	0.735	0.401	0.072	0.184	0.9174
OFAT	21	26	0.121	0.5	0.779	0.380	0.059	0.171	0.9197
GA	21.66	24.01	0.121	0.517	0.769	0.385	0.060	0.167	0.9231 (predicted)

Note: OFAT: one-factor-at-a-time; GA: genetic algorithm.

**Figure 10.** Front and side views of bump configurations. (a) baseline bump; (b) optimized bump.

optimization so that the global maxima for pressure recovery could be identified instead of any local optima. Table 4 shows the input parameters for the implementation of GA, whereas Table 5 shows the comparison of parameters for baseline bump configuration, best configuration determined from OFAT, and optimum design parameters of bump evaluated by GA. It can be observed that the optimized values predicted by GA for A_{\max} is based on corner point, whereas the θ_i , θ_f , and L_{\max} are based on non-corner points. The optimized bump geometry parameters show a slight increase of 3.15% in initial angle of bump and a reduction of 7.65% in bump final angle. The maximum amplitude of bump is reduced by 10.37% for better flow passage, whereas the longitudinal location of bump peak is shifted toward the center. Furthermore, the $A_{T/C}$ for optimized bump is higher than the baseline bump due to its geometric features and results in lower M_{AIP} and flow distortion at the required DMFR. Figure 10 shows the side and front views of baseline and optimized configurations for comparison of geometric features. The predicted total pressure recovery by GA is observed to be 0.9231 which shows a significant improvement in bump performance with respect to baseline bump. The actual performance of optimized bump along with flow characteristics is evaluated in the next section for further verification.

Performance analysis of optimized configuration

The optimized configuration identified by GA is modeled and numerical analysis is carried out to evaluate its performance. Meshing and numerical schemes are kept consistent with the previous cases and the results are compared with baseline bump configuration. For optimized bump, numerical solution is evaluated for supersonic flow speed of $M = 1.6$ and at three different mass flow rates, namely LMFR, DMFR, and high mass flow rate (HMFR).

Flow field analysis at design conditions. Figure 11 shows the shock structure formation at DMFR for baseline bump and optimized bump configurations at $M = 1.6$. For both configurations, the oblique shock can be seen emanating from the compression surface and are impinging on intake cowl lip. When the supersonic flow encounters a concave corner due to bump surface, an oblique shock is generated which results in sharp pressure rise as seen in Figure 11. Due to the pressure rise, the BL tends to increase in thickness and a virtual increase in bump angle is experienced by the flow.¹⁸ As a result, the shock wave is diffused near the bump surface. The oblique shock waves interact with compression waves generated by bump surface along its length and a normal shock is formed at

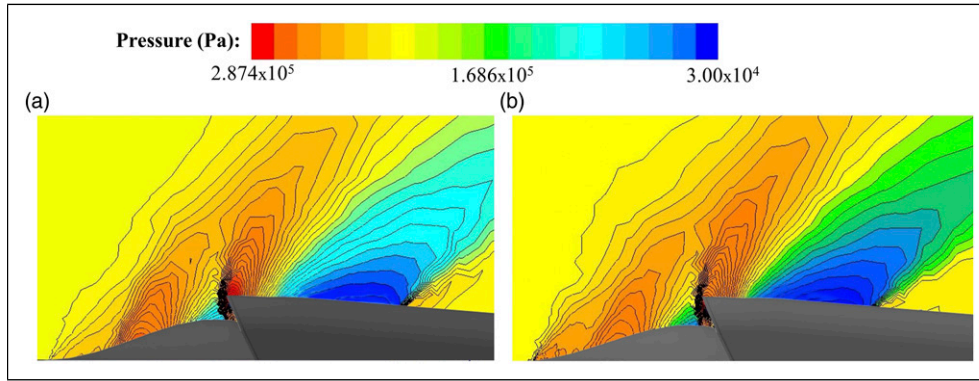


Figure 11. Flow structure around the bump and inlet. (a) baseline bump; (b) optimized bump.

the inlet cowl lip indicated by thick black lines at inlet cowl lip in Figure 11. The lambda normal shock formation can also be observed. For both the configurations, the shock pattern is almost similar; however, slightly weaker shock waves are observed for the optimized bump (Figure 11(b)) than the baseline bump. We further evaluate the intake spillage drag $C_{D_{spill}}$ for both baseline and optimized configurations to ascertain their aerodynamic performance. The $C_{D_{spill}}$ is calculated by

$$C_{D_{spill}} = \frac{(P_i - P_\infty)(A_C - A_\infty)}{q_\infty A_C} \quad (12)$$

where, P_i is the pressure at the inlet of duct, A_C is the inlet capture area, and A_∞ is the inlet mass flow area. A slight reduction in $C_{D_{spill}}$ is observed for optimized configuration as compared to baseline configuration as shown in Table 5. This aspect is further explored by analyzing the flow behavior in the vicinity of bump and inlet cowl for both configurations. The flow field analysis for baseline configuration reveals slightly thicker BL that results in more low energy flow diversion from the inlet than optimized bump. As a consequence, the spillage of baseline configuration is found to be slightly higher than optimized bump. Furthermore, due to higher capture area ratio (A_∞/A_C) for optimized bump, a desired shock on lip condition is met which results in favorable pressure gradient for both the internal and external surfaces of the inlet cowl and creates minimal BL growth. As a result, there is much lower spillage drag for optimized bump. On the other hand, a slightly reduced mass flow rate is observed for baseline bump configuration, and the external flow around the cowl lip is subjected to adverse pressure gradient which leads to higher spillage drag.

Analysis of internal flow inside the inlet duct is as important as the external flow field. To analyze the quality of flow inside the duct and overall performance of inlet, the total pressure at AIP is evaluated for both configurations at $M = 1.6$ and DMFR. For optimized bump (Figure 12(b)), the horizontal pressure distribution at the AIP is observed to be symmetric where a high total pressure region is found at the center of AIP and moderate pressure is observed all around the AIP. A small area of low-pressure region is also observed near the walls which

is attributed to the BL growth inside the walls of the duct and secondary flow due to variation in duct shape. Similar features are observed for baseline bump (Figure 12(a)); however, the area of high pressure is much smaller than the optimized bump, and the low-pressure region near the wall is much widened than the optimized bump. To further evaluate the flow quality quantitatively, the DC is calculated for both baseline and optimized configuration (as shown in Table 5). The DC in this study is defined by the ratio of the difference between the maximum total pressure and mean total pressure by the mean total pressure ($DC = |P_{T,max} - P_{T,mean}|/P_{T,mean}$). A much lower DC is observed for the optimized configuration than baseline configuration. The favorable flow characteristics for the optimized bump can also be attributed to lower M_{AIP} than the baseline bump due to variation in the geometric parameters of the optimized bump. The observed flow features at the AIP for both configurations clearly indicate lower total pressure recovery for baseline bump than optimized bump.

Performance analysis at design and off-design conditions. To analyze the flow structure over the bump surface and inlet duct, pressure variations at different longitudinal sections at the bump symmetry ($y = 0$) are observed at DMFR by evaluating the ratio of static pressure to freestream total pressure at 12 different locations as marked in Figure 13. It is important to note that the longitudinal locations are not equidistant from each other and are carefully selected based on their significance in terms of geometric features and pressure variations. For optimized bump at DMFR condition (in Figure 13), a significant rise in the pressure is observed just at the onset of bump surface (station 2) due to the generated oblique shock waves which also result in BL thickening prior to the formation point of oblique shock waves.³⁸ This phenomenon results in the formation of a virtually wider wedge angle, and the oblique shock waves are diffused near the bump surface which corresponds to smooth pressure rise rather than a sudden jump in pressure. The flow downstream of oblique shock waves experiences a number of compression waves along the bump surface and results in an increase of pressure (station 2–4). A slight reduction in pressure ratio is observed at the rear part of the bump peak at station 5. Prior to the inlet

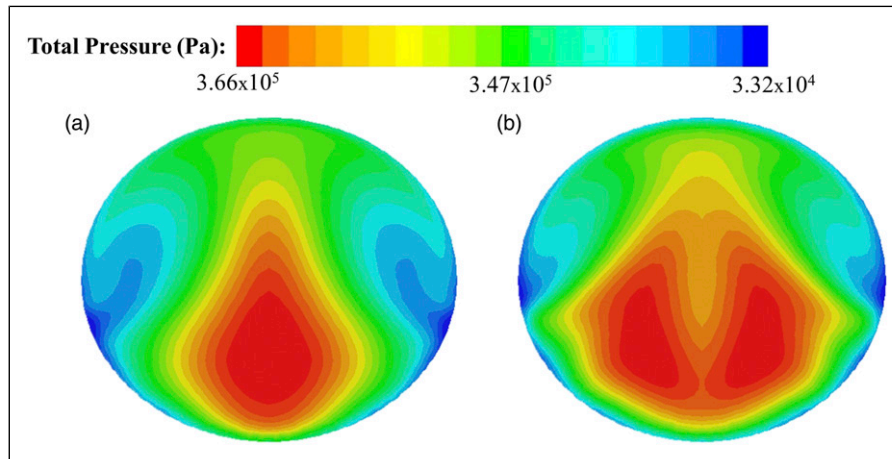


Figure 12. Total pressure at aerodynamic interface plane. (a) baseline bump configuration; (b) optimized bump configuration.

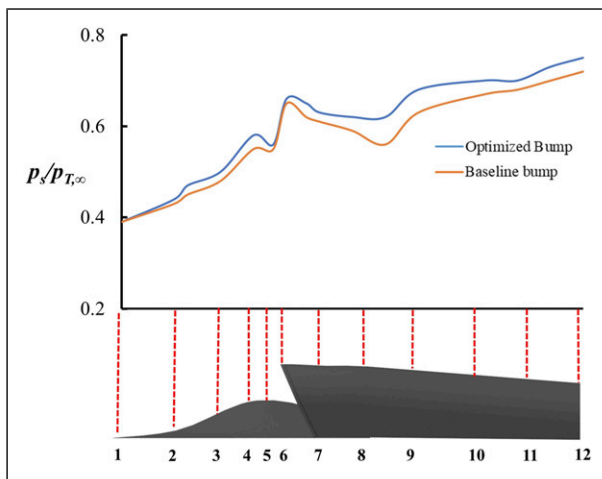


Figure 13. Static pressure distribution along the longitudinal axis at different stations.

entrance, a normal shock is formed resulting in an increase in static pressure (station 6). As a result, the flow is observed to be subsonic inside the duct. The subsonic flow accelerates inside the duct due to the converging area resulting in a pressure reduction (station 6–8), and subsequently, the flow decelerates in the diverging area of duct resulting in a pressure rise (station 9–12). The overall pressure variations along the longitudinal axis are similar to the observations in the experimental work of Soltani and Askari.¹⁸ A similar trend is observed for baseline bump; however, the pressure rise due to the formation of oblique shock waves at the start of bump is weaker than the shock waves observed for the optimized bump. For baseline bump, the overall pressure ratio all along the longitudinal axis is slightly lower than the optimized bump due to higher flow distortion and M_{AIP} for baseline configuration which results in a significant reduction in pressure recovery.

To analyze the effect of off-design conditions on DSI performance, the pressure distribution for optimized bump configuration at DMFR, LMFR, and HMFR are plotted in Figure 14. Characteristics of flow variation for DMFR are already observed in Figure 13. For LMFR, a sharp

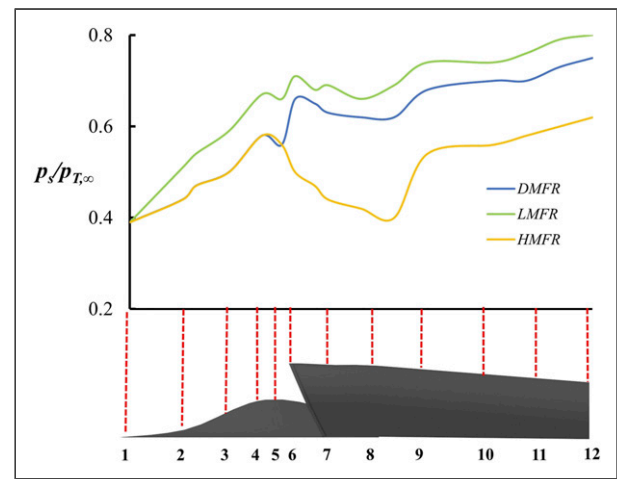


Figure 14. Variation in static pressure along the longitudinal axis for DMFR, LMFR, and HMFR. Note: DMFR: design mass flow rate; LMFR: low mass flow rate.

pressure rise is observed at the bump surface (station 2–4) than the DMFR condition due to the formation of strong oblique shock waves. Furthermore, the rise in static pressure due to normal shock is much less than the DMFR condition indicating the presence of weak normal shock. The observed phenomenon is due to the reduction in mass flow rate which increases the inlet back pressure and alters the flow characteristics inside the duct. As a result of an increase in back pressure, the normal shock from inlet cowl lip is moved upstream toward bump surface which increases the BL thickness in the compression area and results in stronger oblique shock waves and a weak normal shock. The thickening of the BL near the compression surface is undesirable for our designed bump configuration. The observed phenomenon results in flow spillage around the intake and creates spillage drag. Although a rise in pressure ratio and pressure recovery is observed for LMFR condition, the associated spillage drag and BL thickening add more weight to the disadvantages of DSI operation at LMFR. At HMFR condition, the oblique shock formation is similar to DMFR condition (station 1–5).

However, due to HMFR, a low back pressure occurs inside the inlet duct which results in acceleration of flow inside the duct and results in secondary normal shock inside the duct (station 9). This shock is relatively weaker than the normal shock observed at the inlet cowl lip; however, the presence of shock inside the duct adversely affects the pressure recovery and flow characteristics inside the duct. Since the mass flow rate is beyond the design point, the inlet oblique shocks are also ingested inside the cowl lip which adds to flow distortion and subsequently affects the pressure recovery adversely.

Figure 15(a) shows the variation of total pressure recovery at the supersonic speed of $M = 1.6$ with different mass flow rates for baseline and optimized bump configurations. A high-pressure recovery at LMFR is observed for both bump configurations due to the observed phenomenon already discussed in the previous section. The difference between the baseline and optimized bump pressure recovery is almost negligible at LMFR condition. At DMFR, a slight reduction is observed in pressure recovery for both configurations where the reduction in baseline configuration is higher than the optimized bump indicating better performance of our optimized bump at design conditions. At HMFR, a significant reduction in pressure recovery is observed for both configurations due to shock ingestion. The reduction in pressure recovery at HMFR for an optimized bump is much less than baseline bump which indicates that the optimized bump has not only increased the DSI pressure recovery at design

condition but also marginally enhanced the performance of DSI at off-design conditions.

To analyze the effectiveness of the designed optimized bump at different flow speeds, the total pressure recovery at subsonic and supersonic flow speeds are evaluated at DMFR for baseline and optimized bump configuration as shown in Figure 15(b). As expected, the pressure recovery at subsonic flow conditions is higher than the supersonic flow. Interestingly, the optimized bump can maintain slightly better pressure recovery than the baseline bump even in subsonic conditions due to higher $A_{T/C}$ and lower flow distortion (DC). The difference in DSI performance between both configurations becomes prominent at supersonic speeds where the effect of M plays a vital role in lower flow distortion and results in a higher pressure recovery for an optimized bump than its counterpart. The overall trend for baseline and optimized configuration is similar to available literature.^{5,13,16} Nevertheless, the optimized bump has shown much better flow characteristics and performance than the baseline bump for both supersonic and subsonic conditions. Furthermore, the pressure recovery at DMFR for an optimized bump from the numerical analysis is found to be 0.9242 which is almost similar to the predicted pressure recovery by our optimization scheme (0.9231). Hence, the developed design and optimization scheme has not only resulted in a better three-dimensional bump geometry but also can predict the estimated pressure recovery for any new bump design within the established design space.

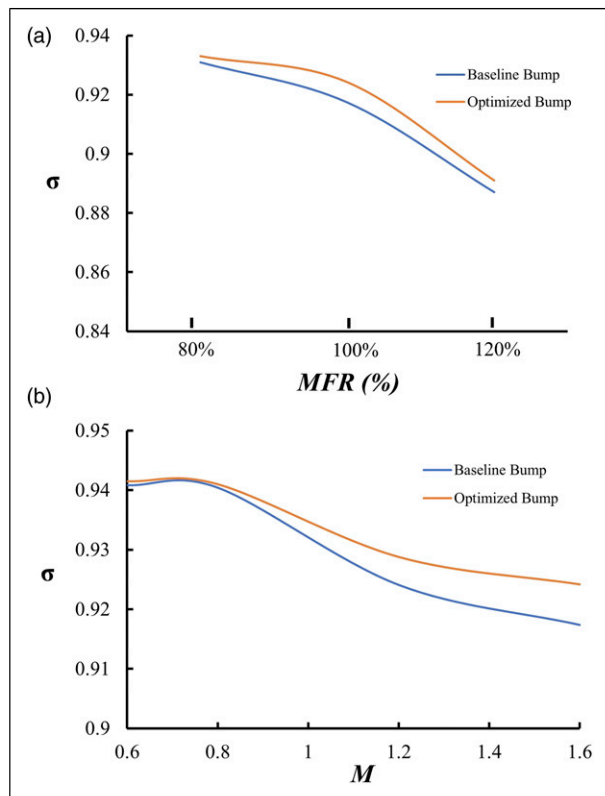


Figure 15. Pressure recovery of baseline and optimized bump. (a) With variation in MFR at $M = 1.6$; (b) With variation in flow speed at DMFR. Note: DMFR: design mass flow rate.

Conclusions

A comprehensive design and optimization scheme of a three-dimensional bump surface for a supersonic jet is developed in this research. A baseline bump in accordance with an existing configuration on a supersonic aircraft is initially modeled and numerical scheme is validated with literature. Design parameters of three-dimensional bump are identified and a design space is established based on sensitivity/uncertainty analysis. A three-level DOE based on design parameters is carried out with a single central point and a total of 25 experiments are designed by Box–Behnken DOE. Subsequently, surrogate modeling is performed to analyze the relationship between parameters and objective function using the least square regression method (LSRM). An excellent correlation is observed between the actual and predicted model by LSRM. The R is observed to be 0.99 and RMSE of only 0.07% is observed which depicts an appropriate fitting model by LSRM. For the optimization of bump design parameters, GA is implemented. The optimized bump geometry parameters resulted in a slight increase of 3.15% in initial angle of bump and a reduction of 7.65% in bump final angle. The maximum amplitude of bump is reduced by 10.37% for better flow passage, whereas the longitudinal location of bump peak is shifted toward the center. The predicted total pressure recovery by GA shows a significant improvement in optimized bump performance with respect to baseline bump. The optimized configuration

identified by GA is modeled and numerical analysis is carried out at DMFR, LMFR, and HMFR. Flow field and performance analysis of optimized bump is performed and compared with baseline configuration which revealed some important favorable flow characteristics for optimized bump which resulted in significant improvement in pressure recovery at supersonic speeds and a slight increase at subsonic speed. The proposed design and optimization methodology can be applied for optimizing the bump surface design of any DSI system for maximizing the intake performance.

Acknowledgements

The authors acknowledge the use of Numerical Analysis Lab. (NAL) of College of Aeronautical Engineering, NUST, Pakistan for numerical simulations.

Declaration of conflicting interests

The author(s) declared no potential conflicts of interest with respect to the research, authorship, and/or publication of this article.

Funding

The author(s) received no financial support for the research, authorship, and/or publication of this article.

ORCID iD

Irsalan Arif  <https://orcid.org/0000-0003-4187-8082>

References

- Mattingly JD. *Elements of Propulsion: Gas Turbines and Rockets*. New York, USA: McGraw-Hill, 2006.
- Soltani MR and Sepahi-Younsi J. Buzz cycle description in an axisymmetric mixed-compression air intake. *AIAA J* 2016; 54(3): 1040–1053.
- Soltani MR, Daliri A and Sepahi Younsi J. Effects of shock wave/boundary-layer interaction on performance and stability of a mixed-compression inlet. *Sci Iran* 2016; 23(4): 1811.
- Seddon J and Goldsmith EL. *Intake aerodynamics*. Oxford: Blackwell science, 1999, Vol. 2.
- Askari R and Soltani MR. Effects of mach number on the performance of a diverterless supersonic inlet. *J Aircr* 2019; 56(4): 1697–1707.
- Hamstra JW and Sylvester TG. *System and Method for Diverting Boundary Layer Air*. United States: Google Patents, 1998.
- Hamstra JW. *Transition Shoulder System and Method for Diverting Boundary Layer Air*. USA: Google Patents, 1998.
- Tillotson BJ, Loth E, Dutton JC, et al. Experimental study of a mach 3 bump-compression flowfield. *J Propul Power* 2009; 25(3): 545–554.
- Loth PC, Brown DW and Huff RG. *Performance of External-Compression Bump Inlet at Mach Numbers of 1.5 to 2.0*. Washington, USA: National Advisory Committee for Aeronautics, 1957.
- Kim SD, Song DJ and Lim S. A numerical analysis on three-dimensional flow field in a supersonic bump inlet. In: 45th AIAA aerospace sciences meeting and exhibit, Reno, Nevada, 08–11 January 2007, 2007.
- Arif I. Flow field analysis of different intake bump (compression surface) configurations on a supersonic aircraft. In: 7th international conference on advances in engineering and technology (AET-17), Phuket, TH, 25–26 May 2017, 2017.
- Askari R and Soltani M. Two-and three-dimensional numerical simulations of supersonic ramped inlet. *Sci Iran Trans B, Mech Eng* 2018; 25(4): 2198–2207.
- B Saheby E, Shen X and Hays AP. Design and performance study of a parametric diverterless supersonic inlet. *Proc Inst Mech Eng G: J Aerosp Eng* 2020; 234(2): 470–489.
- Antonio F. *Scoop-type Supersonic Inlet with Precompression Surface*. USA: Google Patents, 1961.
- Lundy BF, Klinge JD and Leland BC. *System, Method, and Apparatus for Designing Streamline Traced, Mixed Compression Inlets for Aircraft Engines*. USA: Google Patents, 2007.
- Masud J. Flow field and performance analysis of an integrated diverterless supersonic inlet. *Aeronaut J* 2011; 115(1170): 471–480.
- Saheby EB, Guoping H and Hays A. Design of hypersonic forebody with submerged bump. *Proc Inst Mech Eng G: J Aerosp Eng* 2019; 233(9): 3153–3169.
- Soltani MR and Askari R. On the performance of a body integrated diverterless supersonic inlet. *Aerosp Sci Technol* 2019; 91: 525–538.
- Kim SD and Song DJ. Numerical study on performance of supersonic inlets with various three-dimensional bumps. *J Mech Sci Technol* 2008; 22(8): 1640–1647.
- Moin P. *Fundamentals of Engineering Numerical Analysis*. USA: Cambridge University Press, 2010.
- Anderson D, Tannehill JC and Pletcher RH. *Computational Fluid Mechanics and Heat Transfer*. USA: Taylor & Francis, 2016.
- Arif I. Analytical modelling and validation of a turbofan engine at design conditions. In: AIAA scitech 2019 forum, San Diego, CA, 7–11 January 2019, 2019.
- Bulat MP and Bulat PV. Comparison of turbulence models in the calculation of supersonic separated flows. *World Appl Sci J* 2013; 27(10): 1263–1266.
- Kuntz M and Menter F. Simulation of fluid-structure interactions in aeronautical applications. In: *European Congress on Computational Methods in Applied Sciences and Engineering*. Finland: Ecomas Jyväskylä, 2004.
- Yakout M. The selection of process parameters in additive manufacturing for aerospace alloys. *Int J Adv Manuf Technol* 2017; 92(5–8): 2081–2098.
- DeLoach R. Improved quality in aerospace testing through the modern design of experiments. In: 38th aerospace sciences meeting and exhibit, Reno, NV, U.S.A., 10–13 January 2000, 2000.
- Khanna N and Davim JP. Design-of-experiments application in machining titanium alloys for aerospace structural components. *Measurement* 2015; 61: 280–290.
- Mack Y. Surrogate model-based optimization framework: a case study in aerospace design. In *Evolutionary Computation in Dynamic and Uncertain Environments*. Berlin Heidelberg, Germany: Springer, 2007, p. 323–342.
- Ferreira SLC, Bruns RE, Ferreira HS, et al. Box-Behnken design: an alternative for the optimization of analytical methods. *Anal Chim Acta* 2007; 597(2): 179–186.

30. Bruns MA, Meyer JP, Rehman S, et al. Wind power characteristics of seven data collection sites in Jubail, Saudi Arabia using weibull parameters. *Renew Energy* 2017; 102: 35–49.
31. Meyer FA and Schwartz ES. Valuing American options by simulation: a simple least-squares approach. *Rev Financ Stud* 2001; 14(1): 113–147.
32. Dyer JD, Hartfield RJ, Dozier GV, et al. Aerospace design optimization using a steady state real-coded genetic algorithm. *Appl Math Comput* 2012; 218(9): 4710–4730.
33. Hartfield K and Goldberg DE. Control system optimization using genetic algorithms. *J Guid, Control Dyn* 1992; 15(3): 735–740.
34. Mondoloni S. A genetic algorithm for determining optimal flight trajectories. In: Guidance, navigation, and control conference and exhibit, Boston, MA, U.S.A., 10–12 August 1998, 1998.
35. Kamari D, Tadjfar M and Madadi A. Optimization of SD7003 airfoil performance using TBL and CBL at low reynolds numbers. *Aerosp Sci Technol* 2018; 79: 199–211.
36. Nelson D. Numerical optimization of airfoils in low reynolds number flows. *J Aircr* 2009; 46(1): 331–337.
37. Burger C, Hartfield R and Burkhalter J. Propeller performance optimization using vortex lattice theory and a genetic algorithm. In: 44th AIAA aerospace sciences meeting and exhibit, Reno, NV, USA, 9–12 January 2006, 2006.
38. Houghton EL and Carpenter PW. *Aerodynamics for Engineering Students*. Oxford, UK: Elsevier, 2003.

Appendix

Notation

AIP = aerodynamic interface plane

AoA = angle of attack
 A_{\max} = maximum amplitude of bump
 $A_{T/C}$ = throat to capture area ratio
 A_{∞}/A_C = inlet capture area ratio
 $C_{D_{\text{spill}}}$ = spillage drag coefficient
DC = distortion coefficient
DMFR = design mass flow rate
DOE = design of experiment
DSI = diverterless supersonic inlet
GA = Genetic Algorithm
HMFR = high mass flow rate
LMFR = low mass flow rate
LSRM = least square regression method
 L_{\max} = longitudinal location of maximum amplitude of bump
 M = Mach number
OFAT = One-Factor-at-a-Time
RANS = Reynolds-averaged Navier–Stokes equations
RMSE = root mean square error
SA = Spalart–Allmaras turbulence model
 y^+ = non-dimensional length scale associated with turbulence model
 Δy = offset from y -axis
 σ = pressure recovery
 β = shock cone angle
 θ_i = bump initial angle
 θ_T = bump transition angle
 θ_f = bump final angle